



1       **Model-based insights into aerosol perturbation on pristine continental**  
2                               **convective precipitation**

3  
4                   Mengjiao Jiang <sup>1,2</sup>, Yaoting Li <sup>1,3</sup>, Weiji Hu <sup>1</sup>, Yinshan Yang <sup>1,4</sup>, Guy Brasseur <sup>2\*</sup>

5  
6     1, Plateau Atmospheres and Environment Key Laboratory of Sichuan Province & School of  
7     Atmospheric Sciences, Chengdu University of Information Technology, Chengdu 610225, China

8     2, Max Planck Institute for Meteorology, Hamburg 20146, Germany

9     3, Civil Aviation Flight University of China, Guanghan 618307, China

10    4, State Key Laboratory of Earth Surface Processes and Resource Ecology, College of Global  
11    Change and Earth System Science, Beijing Normal University, Beijing 100875, China

12

13    \*Corresponding author: Guy Brasseur (guy.brasseur@mpimet.mpg.de) at Max Planck Institute for  
14    Meteorology, Hamburg 20146, Germany



15

16 **Abstract**

17

18 The Tibetan Plateau (TP) is of great importance for weather and climate due to its role as heat  
19 and water resource. Relatively clean aerosol conditions over the Plateau makes the study on the  
20 aerosol-cloud-precipitation interactions in this pristine continental region distinctive. In order to  
21 investigate the impacts of aerosols on small-scale convection processes over the TP, a convective  
22 event with precipitation observed on 24 July 2014 in Naqu was selected to explore the influence  
23 of aerosols on the onset and intensity of precipitation. We use the Modern-Era Retrospective  
24 analysis for Research and Applications Version 2 (MERRA-2) reanalysis to derive the cloud  
25 condensation nuclei (CCN), which can be regarded as the real-time background. These values are  
26 adopted to initialize the regional WRF 4.0 meteorological model and to simulate the onset of  
27 convective events and the formation of precipitation. Four sets of experiments, named clean (1/10  
28 CCN), control (default setting), Tibetan Plateau (real CCN calculated from MERRA-2 analysis),  
29 and polluted (10 times CCN), were adopted for our simulations. A detailed analysis of  
30 microphysical processes shows that, with the increase in the aerosol number concentration, the  
31 conversion rate of cloud water to rain in clouds is first enhanced. Under polluted situations, the  
32 conversion process of cloud water to rain is suppressed; however, the transformation of cloud  
33 water to graupel and the development of convective clouds are favored. As a result, the onset of  
34 the precipitation is delayed and cold-rain intensity increases.

35

36 **Key words:** Aerosol; Tibetan Plateau; Precipitation

37

38 **Highlights:**

- 39 ● The evolution of convective events on the pristine continental under different atmospheric  
40 aerosol burden are examined.
- 41 ● With the increase in the aerosol number concentration, the conversion of cloud water to rain in  
42 clouds is first enhanced.
- 43 ● Under polluted situations, the onset of the convective precipitation is delayed and the cold-rain  
44 intensity increases.

45



## 46 1. Introduction

47 The role of aerosol particles on the formation of convective clouds and related precipitation  
48 remains a matter of extensive scientific investigations (Andreae et al., 2004; Fan et al., 2013; Freud  
49 and Rosenfeld, 2012; Li et al., 2011; Rosenfeld et al., 2008; Sun and Zhao, 2021; Tao et al., 2012;  
50 Zhao et al., 2020). Due the complexity of the processes involved, the treatment of convective cloud  
51 formation in weather forecast models remains uncertain, especially for the regions with insufficient  
52 observational data. The Tibetan Plateau (TP) represents a relative clean region, in which the  
53 aerosol optical depth baseline value is similar or even lower than that in the Arctic and remote  
54 ocean areas (Pokharel et al., 2019). However, even though the TP is regarded as a pristine continent,  
55 it is occasionally perturbed by the intrusion of dust particles originating in the surrounding deserts  
56 and by black carbon particles produced by biomass burning in the regions of South Asia and part  
57 of Africa (Zhu et al., 2019; Zhao et al., 2020). The analysis presented here in the climate-sensitive  
58 and environmentally fragile continental TP characterized by frequent convective events, will  
59 hopefully be of interest for similar investigations to be conducted in other areas of the world, which  
60 is about the aerosol perturbations on pristine continental.

61 The Tibetan Plateau, with an average elevation of more than 4000 meters, covers  
62 approximately a quarter of the Chinese territory (Wu et al., 2007; Yao et al., 2012). It greatly  
63 influences weather and climate in East Asia and even globally due to its unique geographical  
64 location and topography-induced thermal and dynamical effects (Pokharel et al., 2019). The water  
65 vapor balance on the TP directly affects the water cycle over a large area of the plateau and the  
66 surrounding areas (Duan et al., 2012; Fu et al., 2006; Zhao et al., 2018). Convection on the Tibetan  
67 plateau is characterized by high frequency but low intensity activity (Gao et al., 2016). Aerosols  
68 can act as cloud condensation nuclei (CCN) and ice nuclei (IN) that affect cloud microphysical  
69 processes and thermal and dynamical conditions (IPCC, 2013; Redemann et al., 2021; Stevens et  
70 al., 2017; Yang et al., 2021). Relatively clean conditions with low levels of background aerosols,  
71 frequent convection and induced precipitation make the study of aerosols' impact on convective  
72 precipitation over the TP distinctive.

73 Aerosol observational sites over the TP are sparse. Ground-based observations include (1) the  
74 two stations of the Automated Aerosol Observation Network (AERONET) in Nam Co and  
75 Qomolangma (QOMS), (2) the stations of PM<sub>2.5</sub> and PM<sub>10</sub> from the China Air Quality Online  
76 Monitoring and Analysis Platform (CAWNET) of the Ministry of Environmental Protection at the



77 seven stations of Linzhi, Ali, Lhasa, Changdu, Naqu, Shannan, and Shigatse, and (3) the  
78 concentrations of PM<sub>1</sub> at four stations from China Meteorological Administration (CMA)  
79 Observation Network at Gongga, Lhasa, Xining, and Shangri-La. The monitoring of PM<sub>2.5</sub> and  
80 PM<sub>10</sub> on the TP were initiated in January 2013 at Lhasa, in January 2015 at Ali and Naqu, and in  
81 January 2017 at Changdu, Shannan, Shigatse, and Linzhi. The CMA recorded PM<sub>1</sub> data at Gongga,  
82 Lhasa, and Shangri-La data from January 2014 to December 2018, and at Xining, starting in 2018.  
83 CMA used a GRIMM Model 1.180 aerosol spectrometer with observations every five minutes at  
84 wavelengths ranging from 1 μm to 10 μm. A decade of measurements of aerosol optical properties  
85 at two AERONET stations, Nam Co and QOMS on the Tibetan Plateau, shows that aerosol optical  
86 depth (AOD) values were maximum in spring and minimum in autumn. Due to the anisotropic  
87 reflection of the unique geographical surface in TP, the satellite retrieval of aerosol properties is  
88 difficult (Zhao et al., 2020). The main aerosol types on the Tibetan Plateau were further identified  
89 as continental background, biomass burning, and dust (Pokharel et al., 2019; Zhu et al., 2019; Zhao  
90 et al., 2020). Satellite observations from March to June indicate that aerosols are transported from  
91 South Asia to the region close to the Himalaya (Liu et al., 2008). In summer, aerosols from  
92 Northwest China and Central Asia are transported to the northern Tibetan Plateau (Huang et al.,  
93 2007). In general, aerosol conditions over the TP correspond mainly to a background situation.  
94 However, incoming pollution from South/East Asia under the influence of the summer monsoon  
95 can cause relatively high disturbances in the area of the Tibetan Plateau.

96 Among the studies conducted in development over the TP, are the Third Tibetan Plateau  
97 Atmospheric Scientific Experiment (TIPEX-II and TIPEX-III), initiated jointly by the China  
98 Meteorological Administration (CMA), the Chinese Academy of Sciences (CAS), and the National  
99 Natural Scientific Foundation of China (NSFC) (Zhao et al., 2018), and the Third Pole  
100 Environment (TPE) Program, which was initially proposed and agreed upon by several participants  
101 from China, India, Germany, Japan, Italy, Nepal, the Netherlands, Norway, Pakistan, US, Canada,  
102 Tajikistan, and Switzerland (Yao et al., 2012). These studies highlighted the role of aerosol  
103 characteristics and related impact on cloud and precipitation in TP in relation with weather and  
104 climate modification due to East Asia and South Asia anthropogenic emissions, and dust  
105 mobilization in the Taklamakan Desert (Kang et al., 2019; Liu et al., 2019; Xu et al., 2015), but  
106 also in relation with further impacts on the weather system in the downstream regions, e.g. Yangtze  
107 Delta region, or/and Sichuan Basin (Lau et al., 2019; Liu et al., 2019; Liu et al., 2020; Zhao et al.,



108 2018; Zhao et al., 2020). It has been shown that cloud cover and radiation effects in pristine regions  
109 are particularly sensitive to aerosols (Garrett et al., 2006). Further, aerosols on the Tibetan Plateau  
110 can affect weather and climate directly by absorbing and scattering solar radiation, and indirectly  
111 by modifying the nature of the clouds. Using a cloud-resolving weather research and forecasting  
112 model, Zhou et al. (2017) found that the increase in the aerosol load over the plateau not only  
113 contributes to enhanced updrafts in clouds, but also transports a larger number of ice phase  
114 particles to the upper troposphere. Based on satellite observations and the reanalysis of the dataset,  
115 Liu et al. (2019) studied the effect of aerosols on clouds over the Tibetan Plateau and the effect of  
116 dust-contaminated convective clouds on precipitation in downstream areas. They identified an  
117 effect of Taklamakan dust on convective clouds, which in turn causes heavy rainfall in downstream  
118 areas. However, one should highlight that there are still some uncertainties in the satellite retrievals.  
119 The findings of aerosol-related studies require situation-specific analyses since the northern and  
120 southern parts of the Tibetan Plateau are characterized by different aerosol backgrounds and  
121 composition with different climate systems and meteorological conditions. Using the aerosol  
122 spectral radiative transfer model (SPRINTARS) and the non-hydrostatic Icosahedral Atmospheric  
123 Model (NICAM), Liu et al. (2020) found that dust aerosol transported from the Taklamakan desert  
124 delayed the onset of heavy rainfall in the northern Tibetan Plateau by 12 hours through the indirect  
125 aerosol-cloud interaction, and enhanced the precipitation in the northern region. Aerosols may also  
126 influence the Asian monsoon by affecting snow melting trends and TP surface temperature, which  
127 in turn affects precipitation (Lee et al., 2013). The aerosol impact in the teleconnection between  
128 the “heat-pump” effect (Wu et al., 2016) and the stronger convection and precipitation in the TP  
129 and downstream regions highlight the importance of aerosol perturbation, which need therefore to  
130 be accounted for in the weather forecasting models (Liu et al., 2019; Zhao et al., 2020).

131 Although after decades of efforts, our awareness of Tibetan Plateau aerosols and related  
132 weather impact gradually increased, the confidence of current knowledge on aerosols over the TP  
133 still needs further observational evidence, more in-depth physical analyse and model investigations.  
134 In order to gain understanding on the formation of small-scale convection and related precipitation,  
135 we analyze here a particular event that took place in Naqu ( $92.067^\circ$  E,  $31.483^\circ$  N) on 24 July 2014.  
136 As observational data are sparse, we use the Modern-Era Retrospective analysis for Research and  
137 Applications Version 2 (MERRA-2) reanalysis to derive the cloud condensation nuclei, which can  
138 be regarded as the real-time background. These values are adopted to initialize the regional WRF



139 4.0 meteorological model and to simulate the onset of convective events and the formation of  
140 precipitation. Vertical soundings provide data on the state of the background atmosphere. The  
141 purpose of the present study is to use available information in this region of the Tibetan Plateau to  
142 assess the dependence of the evolution of convective events on the pristine continental under  
143 different background atmospheric aerosol burden. Since data in the region of the Tibetan Plateau  
144 are sparse, the study relies heavily on model simulations, and the outcome should therefore be  
145 regarded a preliminary and partial attempt to investigate a possible relationship between aerosol  
146 and convective precipitation in this region. This methodology could then be applied in other  
147 regions of the world with similar background environments.

148 The paper is organized as follows: Section 2 introduces the data and the methodology that are  
149 adopted in the study; it also describes the convection event under investigation and presents the  
150 experimental design for the numerical simulations. Section 3 compares the microphysical process  
151 that characterize the different model experiments. Section 4 presents a summary and the  
152 conclusions.

153

## 154 **2. Data and methods**

155

### 156 **2.1 Data**

157

#### 158 **2.1.1 MERRA-2 data**

159 MERRA-2, a long-term global reanalysis that assimilates space-based observations of  
160 aerosols (Randles et al., 2017), is an upgrade of the offline aerosol analysis data MERRAero based  
161 on the GOCART model (Chin et al., 2002). GOCART emission sources include aerosols and gases  
162 from biomass burning, fossil fuel combustion, natural emission sources (ocean, volcanic eruptions,  
163 dust), etc. (Chin et al., 2013). The bias-revised AOD is obtained from the observations by the  
164 Moderate Resolution Imaging Spectroradiometer (MODIS). Cloud-filtered Aerosol Robotic  
165 Network (AERONET) AOD data are used as input in a neural network to integrate Moderate  
166 Resolution Imaging Spectroradiometer (MODIS) radiances into the bias-corrected AOD. The  
167 MERRA-2 Aerosol reanalysis data are additionally included in the NASA Earth Observing System  
168 (EOS), NOAA Polar Operational Environmental Satellites (POES), and ground-based  
169 observations (Randles et al., 2017). Note that uncertainties are incurred when satellite retrievals



170 are used over the TP, due to the complicated reflection of the land surface (Yang et al., 2020; Zhao  
171 et al., 2020; Jiang et al., 2022). The dataset used in the present paper is the MERRA-2 aerosol  
172 mixing ratio data MERRA-2 inst3\_3d\_aer\_Nv for 23 July 2014, with a spatial resolution of  $0.625^\circ$   
173  $\times 0.5^\circ$  (longitude, latitude) on 72 vertical layers and with a temporal resolution of 3 hours.

174

### 175 **2.1.2 Precipitation and sounding data**

176 The Station-Satellite combined  $0.1^\circ \times 0.1^\circ$  hourly precipitation data (Shen et al., 2014) are  
177 provided by the China Meteorological Administration Information Center, while the ground  
178 precipitation observations are obtained from the Naqu automatic station. Note that some unrealistic  
179 rainfall centers are depicted over western China due to the sparse automatic weather station  
180 network (Shen et al., 2014). The sounding data are taken from the China Meteorological Data  
181 Network National Meteorological Science Data Center (<http://data.cma.cn>).

182

## 183 **2.2 Method**

184

### 185 **2.2.1 The calculation for cloud condensation nuclei (CCN)**

186 In the Thompson Aerosol-aware scheme (Thompson and Eidhammer, 2014), the number  
187 concentration of cloud droplets is not fixed, but is derived from a series of calculations and look-  
188 up tables of the CCN and IN input calculated from the mixing ratio of different aerosol species.  
189 This scheme takes into account the activation of cloud condensation nuclei to form cloud droplets.  
190 Further, the aerosol background mixing ratios are used to calculate the cloud droplet number  
191 concentration. The input MERRA-2 inst3\_3d\_aer\_Nv data contains the following variables: mass  
192 mixing ratios of sea salt (SS, five bins), sulfate ( $\text{SO}_4$ ), organic carbon (OC), black carbon (BC),  
193 and dust (DU, five bins). The characteristic particle sizes, density parameters, and particle size  
194 ranges were obtained with reference to the aerosol radius distribution file of MERRA-2 (Chin et  
195 al., 2002). We assume that dust particles larger than  $0.5 \mu\text{m}$  are ice-friendly aerosols and that all  
196 remaining aerosol species except black carbon are water-friendly aerosols. The aerosol number  
197 concentrations are calculated at the WRF pre-processing stage by assuming a log-normal  
198 distribution with characteristic diameter and geometric standard deviation in the concentration  
199 (Thompson and Eidhammer, 2014). Since the aerosol radius distribution file of MERRA-2  
200 provides the particle size intervals for different bins of sea salt and dust particles, the integration



201 of the probability density function is determined between the lower and the upper limits of the  
 202 radius. The details of the aerosol parameters are shown in Table 1.

203

204 **Table 1** Aerosol particle radius, standard deviation, and density

Aerosol type	Density (kg m <sup>-3</sup> )	Mean radius (μm)	Radius lower (μm)	Radius upper (μm)	Standard deviation (μm)
Sulfate	1700	0.350	0.005	0.500	2.030
Organic carbon	1800	0.350	0.005	0.500	2.200
	2500	0.730	0.100	1.000	2.000
	2650	1.400	1.000	1.800	2.000
Dust (5 bins)	2650	2.400	1.800	3.000	2.000
	2650	4.500	3.000	6.000	2.000
	2650	8.000	6.000	10.000	2.000
	2200	0.079	0.030	0.100	2.030
Sea salt (5 bins)	2200	0.316	0.100	0.500	2.030
	2200	1.119	0.500	1.500	2.030
	2200	2.818	1.500	5.000	2.030
	2200	7.772	5.000	10.000	2.030

205 The total mass density calculation equation is derived by:

$$\int_{r_{lower}}^{r_{upper}} \frac{N}{r \ln \sigma_g \sqrt{2\pi}} \exp \left[ \frac{-1}{2 \ln^2 \sigma_g} (\ln r - \ln r_g)^2 \right] \frac{4}{3} \pi r^3 \rho dr = M \quad (1)$$

206 where  $N$  is the number concentration,  $r$  is the integral radius,  $\sigma_g$  is the geometric standard  
 207 deviation, and  $r_g$  is the median radius. The probability density integral for selected bin needs to be  
 208 multiplied to the probability  $P$  in the corresponding bin, and it is calculated as:

$$P = \frac{\int_{r_{lower}}^{r_{upper}} \frac{1}{r \ln \sigma_g \sqrt{2\pi}} \exp \left[ \frac{-1}{2 \ln^2 \sigma_g} (\ln r - \ln r_g)^2 \right] dr}{\int_0^{\infty} \frac{1}{r \ln \sigma_g \sqrt{2\pi}} \exp \left[ \frac{-1}{2 \ln^2 \sigma_g} (\ln r - \ln r_g)^2 \right] dr} \quad (2)$$

209 Since ice-friendly aerosols contain only dust aerosol particles with a radius greater than 0.5 μm,  
 210 the percentage of particles with a radius greater than 0.5 μm of the total number of particles in the  
 211 interval is also calculated after the number concentration is derived for the first dust bin. The





212 number concentration of ice-friendly aerosol  $N_i$  and of water-friendly aerosol  
213 concentration  $N_w$  are calculated by Eq. (3) and (4), respectively:

$$N_i = N_{dust1} * P(r_{lower} = 0.5 \mu m) + \sum_{i=2}^5 N_{dusti} \quad (3)$$

214

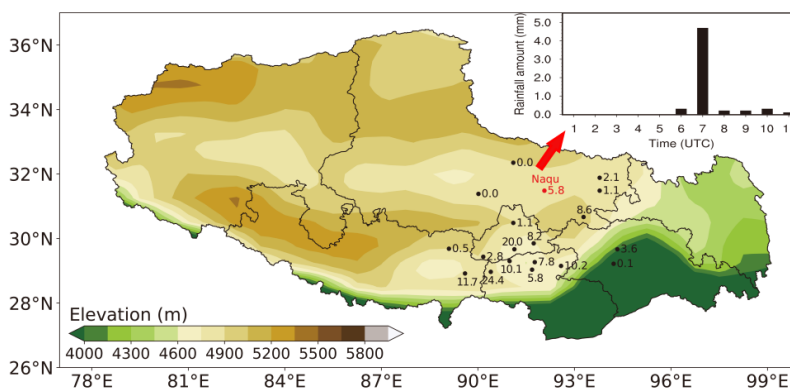
$$N_w = N_{SO4} + N_{OC} + \sum_{i=1}^5 N_{ssi} \quad (4)$$

215 Here  $N_{dusti}$  is the number concentration of dust aerosol particles for five specific bins,  $N_{SO4}$  is the  
216 sulfate number concentration,  $N_{OC}$  is the organic carbon number concentration, and  $N_{ssi}$  is the  
217 number concentration of sea salt particles for five specific bins. The data are interpolated to the  
218 simulation area, and finally written to the WRF Pre-Processing System (WPS).

219

### 220 2.2.2 Case selection

221 The convective precipitation in Naqu on 24 July 2014 is selected for simulation. A mesoscale  
222 precipitation event with a large-scale impact occurred in the central plateau, while the center of  
223 the precipitation area was concentrated in the southern part of the central plateau. The elevation of  
224 the central plateau ranges from 4600 to 5200 meters. As shown in Fig.1, Naqu is located at the  
225 northern edge of this precipitation, and the 24-hour accumulated precipitation amount in Naqu  
226 reaches 5.8 mm. On 24 July, the hourly precipitation amount in 07:00 (UTC) at Naqu station  
227 reached 4.7 mm, which is of medium intensity.

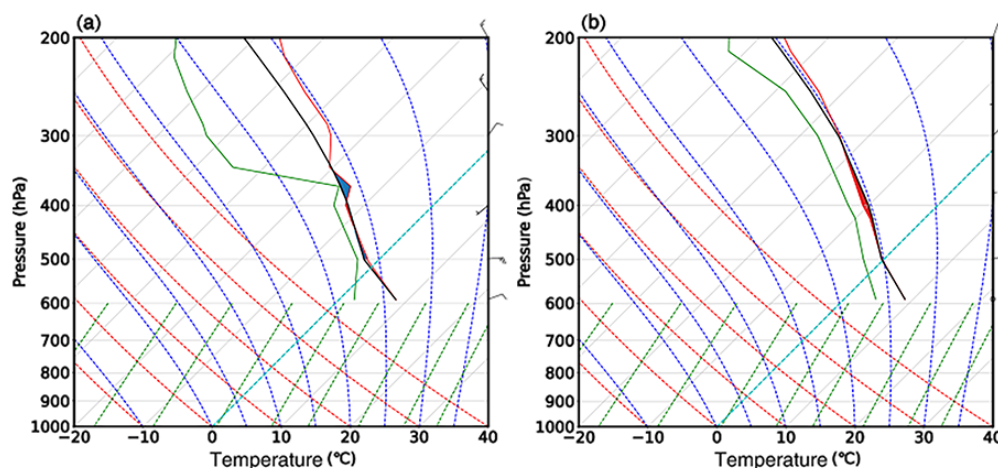


228

229 **Figure 1.** 24-hour accumulated precipitation in Tibet and the hourly precipitation in Naqu on 24  
230 July 2014.



231 From the sounding data map at 00:00 UTC (08:00 at Beijing Time) on 24 July 2014 (Fig. 2a),  
232 the temperature dew point difference in Naqu (red solid line minus green solid line) was less than  
233 4°C, which means that a wet layer was formed between 400-500 hPa. A relatively dry area was  
234 present above 300 hPa, and the whole layer formed an "inverted trumpet" with a dry upper layer  
235 superimposed on a wet lower layer, which is conducive of producing an unstable development of  
236 convection. In Fig. 2b, which corresponds to 12:00 UTC (20:00 at Beijing Time) on the same day,  
237 the relative humidity of the air in the upper troposphere increased significantly and the relative dry  
238 layer disappeared; the whole atmosphere was in a near-saturated state and gradually became stable.  
239 This suggests that the convection developed during 00:00 UTC to 12:00 UTC on 24 July 2014.



240  
241 **Figure 2.** T-logP sounding data from Naqu station at (a) 00:00 UTC and (b) 12:00 UTC on 24  
242 July 2014 (black solid line: temperature-pressure curve (laminar curve); green solid line: dew point  
243 pressure curve; red solid line: state curve; grey solid line (diagonal): isotherm; grey solid line  
244 (straight): isobaric line; blue dashed line: wet adiabatic line; red dashed line: dry adiabatic line;  
245 green dashed line: saturation mixing ratio; light blue dashed line: 0°C isotherm).

246

### 247 2.2.3 Model setup

248 The Weather Research Forecast (WRF) model is one of the most commonly used  
249 meteorological research and numerical weather forecasting systems. It provides users with a wide  
250 choice of formulations for atmospheric processes, and can run on a variety of computer platforms  
251 (<http://www2.mmm.ucar.edu/wrf/users/>). The model version used in this paper is WRF-V4.0, and  
252 the basic model settings are shown in Table 2. The integration of 24 hours starts at 00:00 UTC on



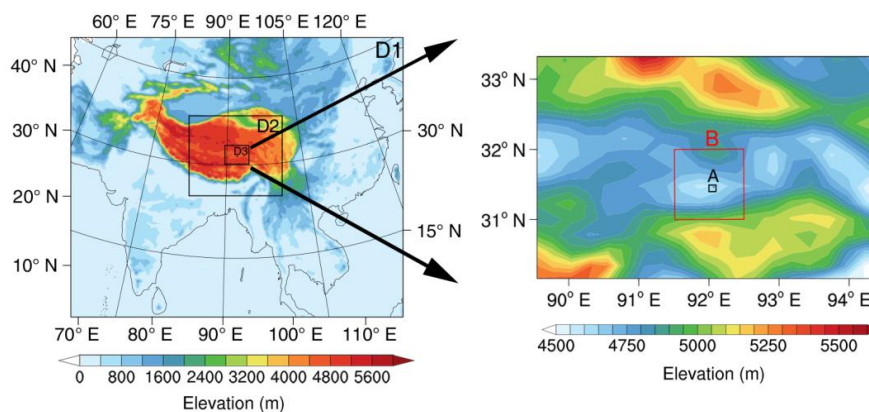
253 24 July 2014. A triple nesting grid with spacing of 25 km, 5 km and 1 km, respectively, and an  
254 integration step of 60 seconds are applied, as shown in Fig.3. The precipitation in the  $0.1^\circ \times 0.1^\circ$   
255 area around Naqu ( $31.4\text{--}31.5^\circ \text{ N}$ ,  $92.0\text{--}92.1^\circ \text{ E}$ , area A) is examined in our detailed analysis.

256

257 **Table 2** Model basic settings

Model basic settings	
Model version	WRF 4.0
Initial field	FNL
Simulation period	24 July 2014 00:00 - 25 July 2014 00:00
Step length	60 s
Number of nesting levels	3 levels
Grid size	25:5:1
Center point	Latitude: $28.0^\circ \text{ N}$ , Longitude: $92.0^\circ \text{ E}$

258



259

260 **Figure 3.** Color-filled map of the height field for simulated region (area A is marked with black  
261 rectangle, and area B is marked with red rectangle).

262 The simulation uses the RRTMG long-wave and short-wave radiation scheme (Iacono et al.,  
263 2008), the Mellor-Yamada-Janjic planetary boundary layer scheme (Dyer et al., 1970), the Eta  
264 similarity near-surface layer scheme, and the Noah-MP land surface scheme (Niu et al., 2011).  
265 The Grell-Freitas cumulus convective parameterization scheme (Grell et al., 2013) is adopted for  
266 the outer two grids while the cumulus scheme is turned off in the inner grid. The physical parameter  
267 schemes are shown in Table 3. The microphysical scheme selected in this paper is the Thompson



268 aerosol-aware scheme (Thompson et al., 2014), in which the default is set as the control run  
269 (Control); the Clean and Polluted schemes multiply the default cloud condensation nuclei number  
270 by 1/10 and 10 times, respectively; the TP uses the MERRA-2 aerosols on 24 July 2014. The  
271 experimental settings are described in Table 4.

272

273 **Table 3** Physical parameter scheme settings

Physical parameter scheme settings	
Microphysical scheme	Thompson aerosol-aware scheme
Long wave radiation scheme	RRTMG Longwave
Shortwave radiation scheme	RRTMG Shortwave
Land surface	Noah-MP
Planetary boundary layer scheme	Mellor-Yamada-Janjic
Cumulus parameterization scheme	Grell-Freitas (the inner layer turns off)

274

275 **Table 4** Experimental settings

Marker	Microphysical settings	Settings
Control	'use_aero_icbc' is set to false	Default NaCCN setting
Clean	'use_aero_icbc' is set to false	1/10*NaCCN
Polluted	'use_aero_icbc' is set to false	10*NaCCN
TP (slightly polluted)	'use_aero_icbc' is set to true	MERRA-2 aerosol reanalysis

276

### 277 **3. Results**

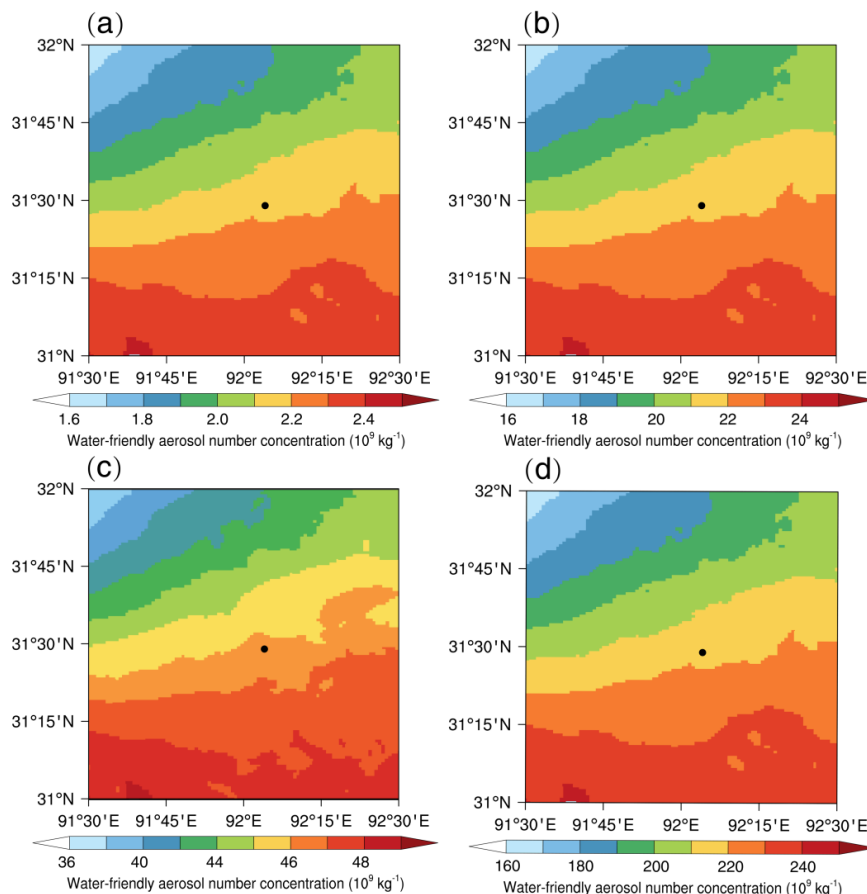
278

#### 279 **3.1 Aerosol and cloud analysis**

280 Figure 4 compares the spatial distribution of the vertically averaged water-friendly aerosol  
281 number concentration from (a) clean, (b) control, (c) TP, and (d) polluted cases at 00:00 on 24 July  
282 2014. It shows that, at the simulation start time, the number concentration of the water-friendly  
283 aerosols in TP simulation (Fig. 4c) is almost 2 times than that of default simulation (Fig. 4b), which  
284 can be regarded as slightly polluted situation. In this way, the dependence of the evolution of the  
285 convective event that took place in Naqu (92.067° E, 31.483° N) on 24 July 2014, are examined  
286 under different background atmospheric aerosol burden, which are almost 1/10, 1 time, 2 times,



287 10 times of the default CCN setting for Clean, Control, TP (slightly polluted), and Polluted,  
288 respectively.



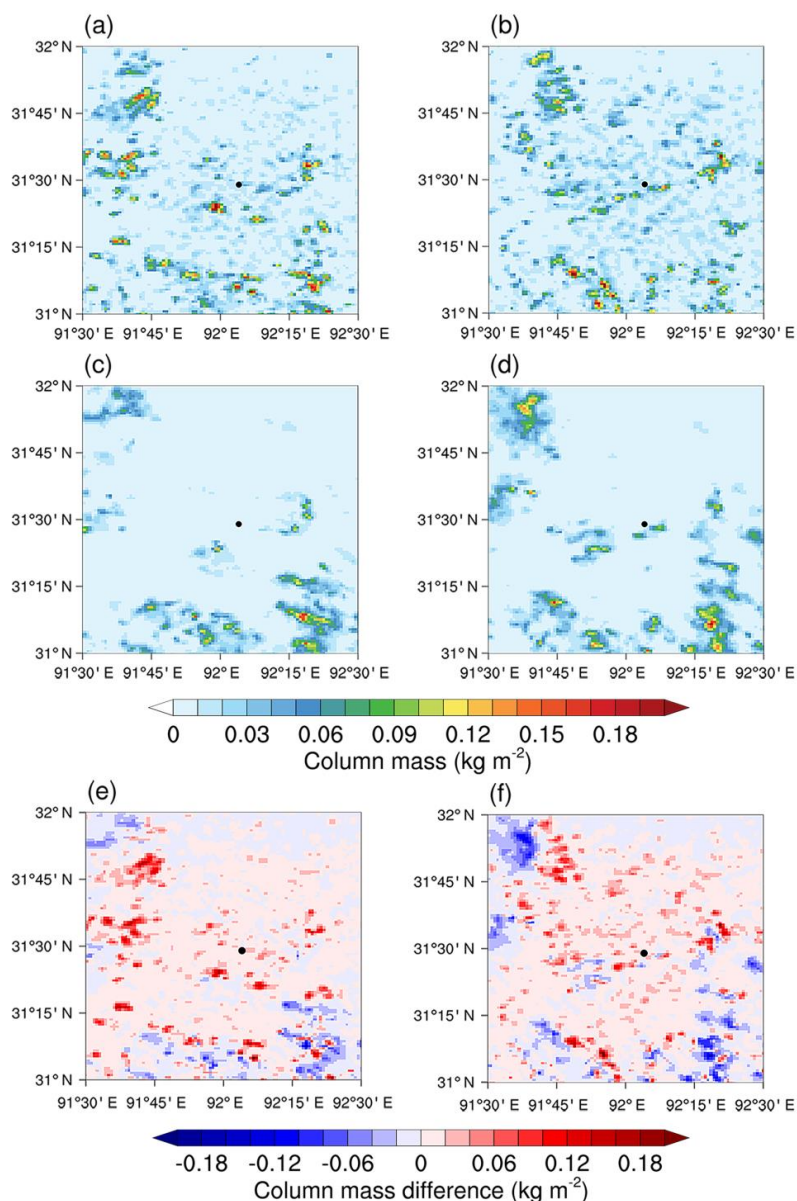
289

290 **Figure 4.** Vertically averaged water-friendly aerosol number concentration from (a) clean, (b)  
291 control, (c) TP, and (d) polluted cases at 00:00 on 24 July 2014. The dot represents the position of  
292 Naqu.

293 Since the precipitation is interrupted at 11:00 UTC (Fig. 1), the analysis focuses on the  
294 vertical distribution of the hydrometeor categories from 00:00 to 11:00 UTC on 24 July 2014. The  
295 column content of each water condensate averaged between 00:00 and 11:00 UTC is represented  
296 in Fig. 5. This figure shows that the content of liquid phase water condensate (Fig. 5a and Fig. 5b)  
297 is significantly higher than the ice phase condensate (Fig. 5c and Fig. 5d) in both clean and polluted  
298 scenarios. It indicates that the event here is a warm-based mixed phase convective cloud, and the  
299 analysis of the vertically pointing Ka-band cloud radar observation at Naqu (Cheng et al., 2021)



300 also validates. The difference of column mass between the liquid phase and ice phase content in  
301 the clean (Fig.5e) and polluted (Fig. 5f) scenarios near Naqu was found to be generally positive,  
302 indicating that the warm cloud process was dominant in this region during the precipitation episode.  
303 When shifting from clean to polluted situations, the ice phase water condensate increases  
304 significantly near Naqu. The regional mean value of this quantity increases by about 37.03% (i.e.,  
305 from  $7.94 \text{ g m}^{-2}$  to  $10.88 \text{ g m}^{-2}$ ), while the regional mean value of liquid phase water content  
306 increases by only 8.45% (i.e., from  $13.49 \text{ g m}^{-2}$  to  $14.63 \text{ g m}^{-2}$ ). This result highlights the  
307 importance of a clean to polluted transition for the ice phase water condensate.

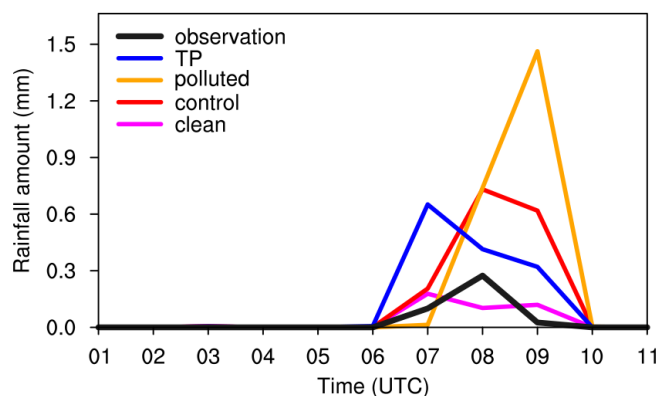


308

309 **Figure 5.** Column content of the vertically integrated mass of (a) liquid phase water condensate  
310 for clean simulation, (b) liquid phase water condensate for polluted simulation, (c) ice phase water  
311 condensate for clean simulation, and (d) ice phase water condensate for polluted simulation. The  
312 difference of column integrated mass between liquid phase and ice phase condensate averaged  
313 from 00:00 to 11:00 on 24 July 2014 for (e) clean, and (f) polluted simulations, units:  $\text{kg m}^{-2}$ .



314 The mean precipitation in the  $0.1^\circ \times 0.1^\circ$  area surrounding Naqu ( $31.4\text{--}31.5^\circ \text{N}$ ,  $92.0\text{--}92.1^\circ$   
315 E, area A) is selected for a time series analysis. Figure 6 shows that the precipitation starts at 06:00  
316 and the hourly maximum precipitation occurs at 08:00. Afterwards, the precipitation intensity  
317 gradually decreases and ends up at 11:00. All four simulations show a decreasing precipitation rate  
318 occurring after 09:00. The maximum precipitation intensity is predicted to happen at 07:00 in the  
319 clean and TP simulations; it occurs at 08:00 and at 09:00 in the control and the polluted simulations,  
320 respectively. The timing of the maximum precipitation rate is delayed and the precipitation  
321 intensity is enhanced as air pollution heavily increases. Comparing the simulation results for clean  
322 and polluted conditions, we find that the time at which precipitation starts occurs later in polluted  
323 air than in relative clean situation. However, the amount of precipitation was significantly  
324 enhanced. This suggests that an increase in atmospheric aerosol load leads to a delayed onset, but  
325 an increased intensity of the precipitation.



326  
327 **Figure 6.** Time series of hourly precipitation rate (mm) in area A ( $31.4\text{--}31.5^\circ \text{N}$ ,  $92.0\text{--}92.1^\circ \text{E}$ ) from  
328 00:00 to 11:00 UTC on 24 July 2014.

329

### 330 3.2 Hydrometeor categories and microphysical processes analysis

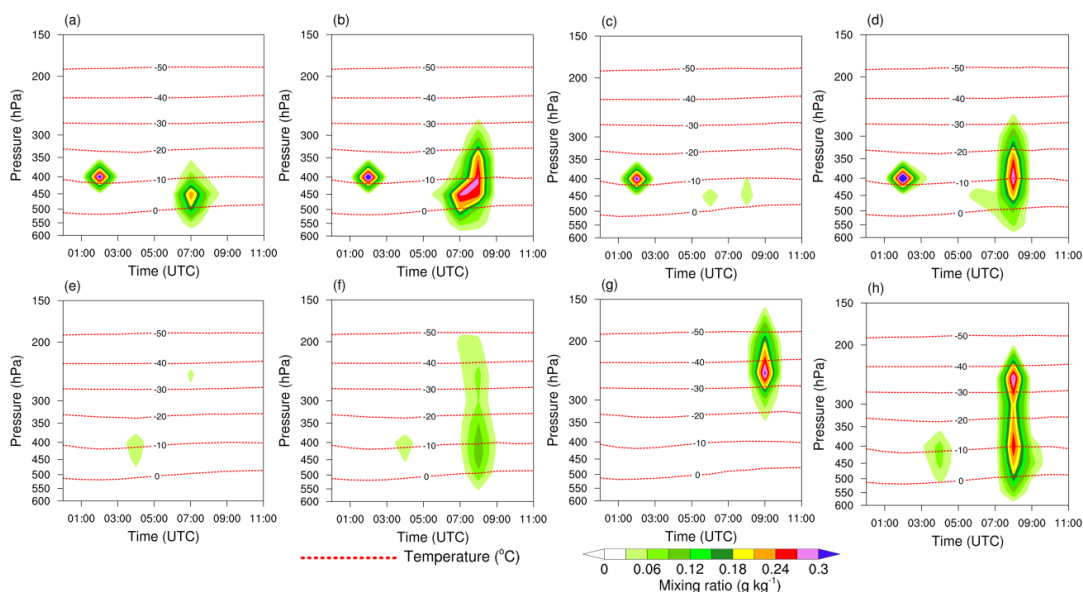
331 In order to analyze the influence of aerosols on water condensate at different heights, the time  
332 series of the vertical distribution of liquid phase water condensate and ice phase water condensate  
333 are shown in Fig. 7, in which, Fig. 7a, b, c, and d are for liquid phase, and Fig. 7e, f, g, and h are  
334 for ice phase. From 01:00 to 03:00, the liquid phase water condensate existed in all four simulated  
335 cases, and were mainly distributed between the pressure levels of 350 and 450 hPa. During this  
336 time, no precipitation was produced or the amount of precipitation was small. The analysis of the





337 vertically pointing Ka-band cloud radar observation at Naqu, also shows that only scattered clouds  
338 existed at the height between 5 and 7 km before 05:00 UTC (Cheng et al., 2021).

339 From 05:00 UTC, the evolution of liquid phase water condensate from clean, control, TP, and  
340 polluted are presented in Fig. 7a, b, c, and d, and the evolution of ice phase water condensate from  
341 clean, control, TP, and polluted are presented in Fig. 7e, f, g, and h, respectively. Note that,  
342 compared to urban areas, the baseline aerosol burden in TP is pristine, and the clean simulation  
343 here represents extremely clean condition. In the clean simulation (Fig. 7a), the liquid phase water  
344 condensate is mainly distributed in the lower layers and its abundance starts to increase, which  
345 indicates the warm-based convective cloud formed; while there little ice phase water condensate  
346 is presented (Fig. 7e). Compared to the clean simulation (Fig. 7a), in the control scenario (Fig. 7b),  
347 the amount of liquid phase water condensate formed in the control case is higher and the maximum  
348 value locates at a higher altitude. At the same time, the ice phase water condensate increases (Fig.  
349 7f). It indicates shifting from clean to control scenario, the convective cloud invigorates and  
350 precipitation increases with increasing aerosol number concentration. In the TP simulation (Fig.  
351 7c), in which the water-friendly aerosols background is 2 times more abundant than in the control  
352 simulation (Fig. 7a), but not in the polluted simulation, the amount of liquid phase water  
353 condensate decreases sharply. This indicates the rain already started (Fig. 6). It also suggests that  
354 the precipitation intensity increases and the precipitation starts earlier with the increase of aerosol  
355 loading when the atmosphere is not heavily polluted. This may be explained by the higher  
356 coalescence efficiency due to the secondary droplet activation in convective clouds, especially in  
357 relatively clean areas (Efraim et al., 2022). In the polluted scenario (Fig. 7d), the liquid phase water  
358 condensate in the polluted case does not change substantially, however, the onset time is delayed.  
359 Under polluted situations, the warm cloud precipitation does not occur easily, and the cloud  
360 development is more vigorous. As a result, the onset time of the precipitation is delayed. The ice  
361 phase water condensate increased substantially. In the polluted case, more ice phase water  
362 condensate is formed in both upper and lower layers (Fig. 7h); while in the TP case (Fig. 7g), there  
363 is more ice phase water condensate only in the upper layers. This suggests that, with the increase  
364 of aerosol loading, the ice cloud precipitation increases. As a result, the onset time of the  
365 precipitation is delayed, but the precipitation intensity increases. This is consistent with the impact  
366 of aerosols on convective precipitation as derived from observations in China (Jiang et al., 2016).



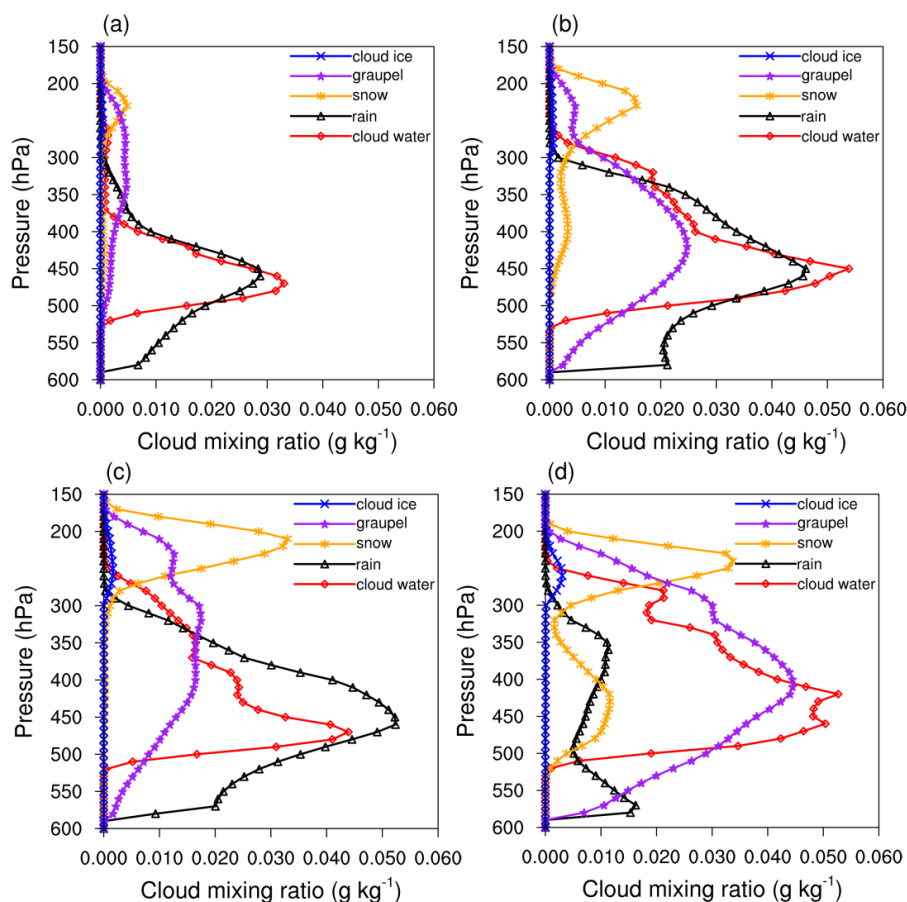
367

368 **Figure 7.** Time series of the vertical distribution of the mean liquid phase water (upper 4 sub-plots)  
369 condensate mixing ratio in (a) clean, (b) control, (c) TP, and (d) polluted, and ice phase  
370 (bottom 4 subplots) in (e) clean, (f) control, (g) TP, and (h) polluted in area A (31.4-31.5°N,92.0-  
371 92.1°E), in  $\text{g kg}^{-1}$ , with red dashed lines as isotherms.

372 In order to analyze the evolution of microphysical quantities and processes, considering that  
373 precipitation mainly occurs between 06:00 and 11:00, various water condensate particles in area  
374 A are averaged between 06:00 and 11:00. Five water condensate mixing ratios varying with height  
375 are obtained for cloud water, cloud ice, rain, snow, and graupel are shown in Figure 8. The water  
376 condensate mixing ratios for clean, control, TP, and polluted simulations are presented in Fig. 8a,  
377 b, c, and d, respectively. At 150-300 hPa, snowfall occurs in all four scenarios, and the proportion  
378 of snowfall increases as pollution increases. At 300-500hPa, compared with the clean simulation  
379 (Fig. 8a), the water condensate mixing ratio of cloud water, cloud ice, rain, snow, and graupel  
380 increase with the increased aerosol burden in the control simulation (Fig. 8b). Compared with the  
381 control simulation (Fig. 8b), the mixing ratio of rain increases while both of cloud water and  
382 graupel decrease in the TP simulation (Fig. 8c). This suggests that, as aerosol loading increases,  
383 the conversion process of cloud water to rain invigorates at first. In the polluted scenario (Fig. 10d),  
384 the mixing ratios of cloud water, graupel, and snow are characterized by larger values than in the  
385 other three scenarios, while the mixing ratio of rain has the smallest value. It indicates that the



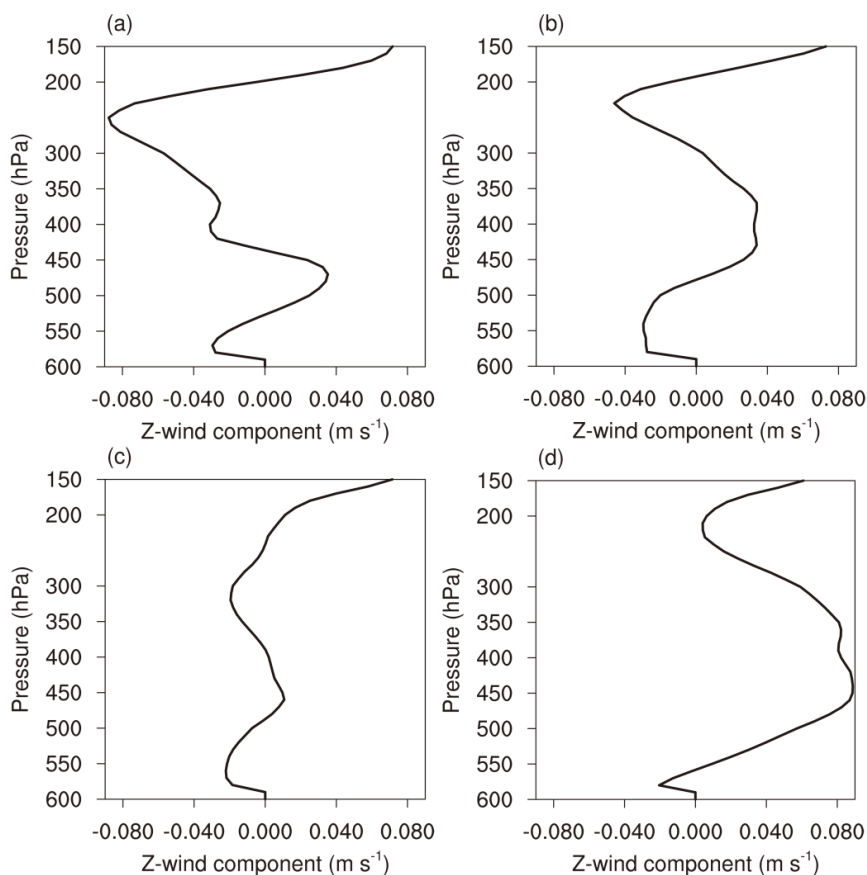
386 conversion process of cloud water to rain is suppressed, but the conversion of cloud water to  
387 graupel is favored. At 500-600 hPa, which is near the surface, rainfall is dominant in the clean case  
388 (Fig. 8a), while graupel in addition to rainfall are visible in other cases (Fig. 8b, c, and d). The  
389 proportion of graupel increases and the proportion of rain decreases. This suggests that, with the  
390 increase of aerosol burden, the conversion process of cloud water to rain in clouds is suppressed,  
391 but the generation of ice phase particles is favored. This also indicates that the development of  
392 convective clouds is more vigorous under the polluted scenario.



393  
394 **Figure 8.** Mean water condensate mixing ratio as a function of height for (a) clean, (b) control, (c)  
395 TP, and (d) polluted cases in area A (31.4-31.5°N, 92.0-92.1°E) from 06:00 to 11:00 UTC on 24  
396 July 2014, units:  $\text{g kg}^{-1}$ .



397 The vertical distributions of the number concentration of cloud water, rain and snow for the  
398 four scenarios (which is not shown here) show similar results, which indicates the increase of  
399 aerosol number concentration tends to increase the cloud droplet number concentration but to  
400 decrease the cloud droplet scale, suppresses the warm cloud rainfall and invigorates cloud  
401 development (Fig. 9), producing more ice phase substances. The melting of ice phase particles  
402 increases the cold-rain precipitation, which delays the onset of the precipitation and increases  
403 precipitation intensity. It is consistent with the findings that in polluted scenario, the increase in  
404 aerosols suppress the warm-rain process but enhance the growth of hail and increase the cold-rain  
405 (Rosenfeld et al., 2000; Tao et al., 2012).



406 **Figure 9.** Vertical velocity for the (a) clean, (b) control, (c) TP, and (d) polluted cases in area A  
407 (31.4–31.5°N, 92.0–92.1°E) averaged from 06:00 to 11:00 UTC on 24 July 2014, in units of  $\text{m s}^{-1}$ .  
408  
409



#### 410 **4. Summary and discussion**

411

412 Aerosol studies on the Tibetan Plateau are constrained by a small number of stations and  
413 observations, and by a limited amount of satellite data. In this region characterized by clean air  
414 conditions, the aerosol optical thickness is generally smaller than in other regions, with only a few  
415 cases exceeding 0.1, which also explains the low availability of aerosol satellite data in the region.  
416 Although the region can be viewed as a region with a background aerosol situation, air masses  
417 transported by summer winds from South Asia can cause relatively strong local disturbances.  
418 Therefore, it is an ideal region to examine the aerosol impact on convective precipitation and on  
419 the downstream weather. The unique topography and the relatively pristine aerosol background  
420 levels above the Tibetan Plateau motivate us to explore the impact of high aerosol episodes on the  
421 formation of local convective precipitation events.

422 The Weather Research and Forecasting (WRF) model 4.0 version with Thompson aerosol-  
423 aware microphysical scheme was used to explore the influence of aerosols on convective  
424 precipitation processes. A specific convective precipitation event in Naqu, on the central Tibetan  
425 Plateau that occurred on 24 July 2014 was selected in our study. Four sets of experiments, named  
426 clean (1/10 CCN), control (default setting), Tibetan Plateau (real CCN calculated from MERRA-  
427 2 reanalysis), and polluted (10 times CCN), were retained for our simulations. A detailed analysis  
428 on microphysical processes suggests that, with the increase of the aerosol number concentration,  
429 the conversion of cloud water to rain inside clouds is enhanced at first, while in polluted situation,  
430 the conversion process of cloud water to rain is suppressed. At the same time, the generation of  
431 ice phase particles and the development of convective clouds are enhanced. In polluted situation,  
432 the onset of the precipitation is delayed; however, rainfall occurs with higher intensity.

433 Since the air in the plateau area is relatively clean, the response of precipitation could be  
434 sensitive to aerosol perturbation. However, the errors associated with the observations over the  
435 Tibetan Plateau are large and sensitive to convective precipitation during the initial phase of the  
436 event. Under such circumstances, our study has adopted a compromise approach to discuss the  
437 effect of aerosols on convective precipitation in the relatively clean highland/pristine continent.

438 The treatment of aerosols in the model can be chosen according to the air quality situation at  
439 a particular time. If the air is clean, initial conditions for the simulated aerosol concentrations can  
440 be chosen to be close to the actual observations; in a polluted situation, the background field for



441 the WRF simulation can be generated according to the real-time aerosol reanalysis method as  
442 described in the paper, especially before year 2015. More sustained and comprehensive  
443 observations over the Tibetan Plateau are a prerequisite for better understanding the aerosol impact  
444 on precipitation formation in this region. At the same time, approaches to determining  
445 measurement representation error (Asher et al., 2022) for model evaluation should be established  
446 in the pristine region .



447 **Data Availability**

448 The Station-Satellite combined  $0.1^\circ \times 0.1^\circ$  hourly precipitation data (Shen et al., 2014) are  
449 provided by the China Meteorological Administration Information Center, and the ground  
450 precipitation observations are obtained from the Naqu automatic station. The sounding data are  
451 taken from the China Meteorological Data Network National Meteorological Science Data Center.  
452 All the data is available at (<http://data.cma.cn>).



453

454 **Acknowledgments**

455

456 This study was supported by the National Key Research and Development Program of China  
457 (2018YFC1505704), the National Natural Science Foundation of China (41905025), and the China  
458 Scholarship Council. We would like to thank the Chinese Meteorological Administration's  
459 National Meteorological Information Center (<http://cdc.cmic.cn>, and <http://data.cma.cn/>), Dr.  
460 Wenhua Gao from the State Key Laboratory of Severe Weather, Chinese Academy of  
461 Meteorological Sciences, and Dr. Xiaolong Cheng from the Institute of Plateau Meteorology,  
462 China Meteorological Administration, Dr. Xiaoling Zhang from Chengdu Plain Urban  
463 Meteorology and Environment Observation and Research Station of Sichuan Province, for their  
464 suggestions that have benefited this study. We also greatly appreciate the valuable comments from  
465 the anonymous reviewers.





466 **References**

467

468 Asher, E., Thornberry, T., Fahey, D. W., McComiskey, A., Carslaw, K., Grunau, S., Chang, K. L.,  
469 Telg, H., Chen, P., and Gao, R. S.: A Novel Network-Based Approach to Determining  
470 Measurement Representation Error for Model Evaluation of Aerosol Microphysical  
471 Properties, *J. Geophys. Res.-Atmos.*, 127, e2021JD035485,  
472 <https://doi.org/10.1029/2021JD035485>, 2022.

473 Cheng, X., Shi, Y., and Gao, W.: A Study of One Local-Scale Convective Precipitation Event  
474 Over Central Tibetan Plateau with Large Eddy Simulations, *Earth and Space Science*, 9,  
475 e2021EA001870, <https://doi.org/10.1029/2021EA001870>, 2022.

476 Chin, M., Ginoux, P., Kinne, S., Torres, O., Holben, B. N., Duncan, B. N., Martin, R. V., Logan,  
477 J. A., Higurashi, A., and Nakajima, T.: Tropospheric aerosol optical thickness from the  
478 GOCART model and comparisons with satellite and Sun photometer measurements, *J.*  
479 *Atmos. Sci.*, 59, 461-483, [https://doi.org/10.1175/1520-](https://doi.org/10.1175/1520-0469(2002)059<0461:TAOTFT>2.0.CO;2)  
480 [0469\(2002\)059<0461:TAOTFT>2.0.CO;2](https://doi.org/10.1175/1520-0469(2002)059<0461:TAOTFT>2.0.CO;2), 2002.

481 Chin, M., Diehl, T., Tan, Q., Prospero, J., Kahn, R., Remer, L., Yu, H., Sayer, A., Bian, H., and  
482 Geogdzhayev, I.: Multi-decadal aerosol variations from 1980 to 2009: a perspective from  
483 observations and a global model, *Atmos. Chem. Phys.*, 14, 3657-3690,  
484 <https://doi.org/10.5194/acp-14-3657-2014>, 2014.

485 Duan, A., Wu, G., Liu, Y., Ma, Y., and Zhao, P.: Weather and climate effects of the Tibetan Plateau,  
486 *Adv. Atmos. Sci.*, 29, 978-992, <https://doi.org/10.1007/s00376-012-1220-y>, 2012.

487 Dyer, A. and Hicks, B.: Flux-gradient relationships in the constant flux layer, *Q. J. Roy. Meteor.*  
488 *Soc.*, 96, 715-721, <https://doi.org/10.1002/qj.49709641012>, 1970.

489 Efraim, A., Lauer, O., Rosenfeld, D., Braga, R. C., Franco, M.-A., Kremper, L.A., Zhu, Y.,  
490 Pöschl, U., Pöhlker, C., Andreae, M. O., Artaxo, Araújo, P. A., Pöhlker, M.L.: Satellite-  
491 based detection of secondary droplet activation in convective clouds, *J. Geophys. Res.-*  
492 *Atmos.*, 127, e2022JD036519, <https://doi.org/10.1029/2022JD036519>, 2022.

493 Fu, Y., Liu, G., Wu, G., Yu, R., Xu, Y., Wang, Y., Li, R., and Liu, Q.: Tower mast of precipitation  
494 over the central Tibetan Plateau summer, *Geophys. Res. Lett.*, 33,  
495 <https://doi.org/10.1029/2005GL024713>, 2006.



- 496 Gao, W., Sui, C. H., Fan, J., Hu, Z., and Zhong, L.: A study of cloud microphysics and precipitation  
497 over the Tibetan Plateau by radar observations and cloud-resolving model simulations, *J.*  
498 *Geophys. Res.-Atmos.*, 121, 13,735-13,752, <https://doi.org/10.1002/2015JD024196>, 2016.
- 499 Garrett, T. J. and Zhao, C.: Increased Arctic cloud longwave emissivity associated with pollution  
500 from mid-latitudes, *Nature*, 440, 787-789, <https://doi.org/10.1038/nature04636>, 2006.
- 501 Grell, G. A. and Freitas, S. R.: A scale and aerosol aware stochastic convective parameterization  
502 for weather and air quality modeling, *Atmos. Chem. Phys.*, 14, 5233-5250,  
503 <https://doi.org/10.5194/acp-14-5233-2014>, 2014.
- 504 Huang, J., Minnis, P., Yi, Y., Tang, Q., Wang, X., Hu, Y., Liu, Z., Ayers, K., Treppe, C., and  
505 Winker, D.: Summer dust aerosols detected from CALIPSO over the Tibetan Plateau,  
506 *Geophys. Res. Lett.*, 34, <https://doi.org/10.1029/2007GL029938>, 2007.
- 507 Iacono, M. J., Delamere, J. S., Mlawer, E. J., Shephard, M. W., Clough, S. A., and Collins, W. D.:  
508 Radiative forcing by long-lived greenhouse gases: Calculations with the AER radiative  
509 transfer models, *J. Geophys. Res.-Atmos.*, 113, <https://doi.org/10.1029/2008jd009944>, 2008.
- 510 Intergovernmental Panel on Climate Change: Climate Change 2013: The Physical Science Basis,  
511 in Contribution of Working Group I to the Fifth Assessment Report of the Intergovernmental  
512 Panel on Climate Change, Cambridge Univ. Press, Cambridge, UK, 2013.
- 513 Jiang, M., Chen, Z., Yang, Y., Ni, C., and Yang, Q.: Establishment of aerosol optical depth dataset  
514 in the Sichuan Basin by the random forest approach, *Atmos. Pollut. Res.*, 13(5), 101394,  
515 <https://doi.org/10.1016/j.apr.2022.101394>, 2022.
- 516 Jiang, M., Li, Z., Wan, B., and Cribb, M.: Impact of aerosols on precipitation from deep convective  
517 clouds in eastern China, *J. Geophys. Res.-Atmos.*, 121, 9607-9620,  
518 <https://doi.org/10.1002/2015JD024246>, 2016.
- 519 Kang, S., Zhang, Q., Qian, Y., Ji, Z., Li, C., Cong, Z., Zhang Y., Guo J., Du W., Huang J., You  
520 Q., Panday A.-K., Rupakheti M., Chen, D., Gustafsson, Ö., Thiemens, M.-H., Qin, D.:  
521 Linking atmospheric pollution to cryospheric change in the Third Pole region: current  
522 progress and future prospects, *Natl. Sci. Rev.*, 6, 796-809, <https://doi.org/10.1093/nsr/nwz031>,  
523 2019.
- 524 Kaufman, Y. J., Koren, I., Remer, L.A., Rosenfeld, D., Rudich, Y.: The effect of smoke, dust, and  
525 pollution aerosol on shallow cloud development over the Atlantic Ocean, *Proc. Natl. Acad.*  
526 *Sci.*, 102, 11207-11212, <https://doi.org/10.1073/pnas.0505191102>, 2005.



- 527 Koren, I., Martins, J. -V., Remer, L.-A., Afargan, H.: Smoke Invigoration Versus Inhibition of  
528 Clouds over the Amazon, *Science*, 321, 946–949, <https://doi.org/10.1126/science.1159185>,  
529 2008.
- 530 Lau, W., Kim, K.-M.: Impact of Snow Darkening by Deposition of Light-Absorbing Aerosols on  
531 Snow Cover in the Himalayas–Tibetan Plateau and Influence on the Asian Summer Monsoon:  
532 A Possible Mechanism for the Blanford Hypothesis, *Atmosphere*, 9, 438,  
533 <https://doi.org/10.3390/atmos9110438>, 2018.
- 534 Lee, W.-S., Bhawar, R. L., Kim, M.-K., and Sang, J.: Study of aerosol effect on accelerated snow  
535 melting over the Tibetan Plateau during boreal spring, *Atmos. Environ.*, 75, 113-122,  
536 <https://doi.org/10.1016/j.atmosenv.2013.04.004>, 2013.
- 537 Liu, Y., Zhu, Q., Huang, J., Hua, S., and Jia, R.: Impact of dust-polluted convective clouds over  
538 the Tibetan Plateau on downstream precipitation, *Atmos. Environ.*, 209, 67-77,  
539 <https://doi.org/10.1016/j.atmosenv.2019.04.001>, 2019.
- 540 Liu, Y., Zhu, Q., Hua, S., Alam, K., Dai, T., and Cheng, Y.: Tibetan Plateau driven impact of  
541 Taklimakan dust on northern rainfall, *Atmos. Environ.*, 234, 117583,  
542 <https://doi.org/10.1016/j.atmosenv.2020.117583>, 2020.
- 543 Liu, Z., Liu, D., Huang, J., Vaughan, M., Uno, I., Sugimoto, N., Kittaka, C., Treppe, C., Wang, Z.,  
544 and Hostetler, C.: Airborne dust distributions over the Tibetan Plateau and surrounding areas  
545 derived from the first year of CALIPSO lidar observations, *Atmos. Chem. Phys.*, 8, 5045-  
546 5060, <https://doi.org/10.5194/acp-8-5045-2008>, 2008.
- 547 Niu, G. Y., Yang, Z. L., Mitchell, K. E., Chen, F., Ek, M. B., Barlage, M., Kumar, A., Manning,  
548 K., Niyogi, D., and Rosero, E.: The community Noah land surface model with  
549 multiparameterization options (Noah-MP): 1. Model description and evaluation with local-  
550 scale measurements, *J. Geophys. Res.-Atmos.*, 116, <https://doi.org/10.1029/2010jd015139>,  
551 2011.
- 552 Pokharel, M., Guang, J., Liu, B., Kang, S., Ma, Y., Holben, B. N., Xia, X. a., Xin, J., Ram, K., and  
553 Rupakheti, D.: Aerosol properties over Tibetan Plateau from a decade of AERONET  
554 measurements: baseline, types, and influencing factors, *J. Geophys. Res.-Atmos.*, 124,  
555 13357-13374, <https://doi.org/10.1029/2019JD031293>, 2019.
- 556 Randles, C., Da Silva, A., Buchard, V., Colarco, P., Darmenov, A., Govindaraju, R., Smirnov, A.,  
557 Holben, B., Ferrare, R., and Hair, J.: The MERRA-2 aerosol reanalysis, 1980 onward. Part I:



- 558 System description and data assimilation evaluation, *J. Clim.*, 30, 6823-6850,  
559 <https://doi.org/10.1175/JCLI-D-16-0609.1>, 2017.
- 560 Redemann, J., Wood, R., Zuidema, P., Doherty, S. J., Luna, B., LeBlanc, S. E., Diamond, M. S.,  
561 Shinozuka, Y., Chang, I. Y., and Ueyama, R.: An overview of the ORACLES (Observations  
562 of Aerosols above Clouds and their interactions) project: aerosol–cloud–radiation interactions  
563 in the southeast Atlantic basin, *Atmos. Chem. Phys.*, 21, 1507-1563,  
564 <https://doi.org/10.5194/acp-21-1507-2021>, 2021.
- 565 Rodriguez-Caballero, E., Stanelle, T., Egerer, S., Cheng, Y., Su, H., Canton, Y., Belnap, J.,  
566 Andreae, M.O., Tegen, I., Reick, C. H., Pöschl, U., Weber, B.: Global cycling and climate  
567 effects of aeolian dust controlled by biological soil crusts, *Nat. Geosci.*, 15, 1-6,  
568 <https://doi.org/10.1038/s41561-022-00942-1>, 2022.
- 569 Rosenfeld D, Lensky I M.: Satellite-based insights into precipitation formation processes in  
570 continental and maritime convective clouds, *B. Am. Meteorol. Soc.* 79, 2457-2476,  
571 [https://doi.org/10.1175/1520-0477\(1998\)079<2457:SBIIPF>2.0.CO;2](https://doi.org/10.1175/1520-0477(1998)079<2457:SBIIPF>2.0.CO;2), 1998.
- 572 Rosenfeld, D. and Woodley, W. L.: Deep convective clouds with sustained supercooled liquid  
573 water down to -37.5 degrees C, *Nature*, 405, 440-442, <https://doi.org/10.1038/35013030>, 2000.
- 574 Rosenfeld D, Rudich Y, Lahav R.: Desert dust suppressing precipitation: A possible desertification  
575 feedback loop, *Proc. Natl. Acad. Sci.*, 98, 5975-5980,  
576 <https://doi.org/10.1073/pnas.101122798>, 2001.
- 577 Rosenfeld D., Lohmann U., Raga G.B., O'Dowd, C.D., Kulmala, M., Fuzzi, S., Reissell, A.,  
578 Andreae, M.O.: Flood or drought: how do aerosols affect precipitation?, *Science*, 321, 1309-  
579 1313, <https://doi.org/10.1126/science.1160606>, 2008.
- 580 Shen, Y., Zhao, P., Pan, Y., and Yu, J.: A high spatiotemporal gauge-satellite merged precipitation  
581 analysis over China, *J. Geophys. Res.-Atmos.*, 119, 3063-3075,  
582 <https://doi.org/10.1002/2013JD020686>, 2014.
- 583 Stevens, B., Fiedler, S., Kinne, S., Peters, K., Rast, S., Müsse, J., Smith, S. J., and Mauritsen, T.:  
584 MACv2-SP: A parameterization of anthropogenic aerosol optical properties and an associated  
585 Twomey effect for use in CMIP6, *Geosci. Model. Dev.*, 10, 433-452,  
586 <https://doi.org/10.5194/gmd-10-433-2017>, 2017.



- 587 Sun, Y., and Zhao, C.: Distinct impacts on precipitation by aerosol radiative effect over three  
588 different megacity regions of eastern China, *Atmos. Chem. Phys.*, 21, 16555-16574,  
589 <https://doi.org/10.5194/acp-21-16555-2021>, 2021.
- 590 Tao, W. K., Chen, J. P., Li, Z., Wang, C., and Zhang, C.: Impact of aerosols on convective clouds  
591 and precipitation, *Rev. Geophys.*, 50, <https://doi.org/10.1029/2011RG000369>, 2012.
- 592 Thompson, G. and Eidhammer, T.: A study of aerosol impacts on clouds and precipitation  
593 development in a large winter cyclone, *J. Atmos. Sci.*, 71, 3636-3658,  
594 <https://doi.org/10.1175/JAS-D-13-0305.1>, 2014.
- 595 Wu, G., Liu, Y., Zhang, Q., Duan, A., Wang, T., Wan, R., Liu, X., Li, W., Wang, Z., and Liang,  
596 X.: The influence of mechanical and thermal forcing by the Tibetan Plateau on Asian climate,  
597 *J Hydrometeorol*, 8, 770-789, <https://doi.org/10.1175/JHM609.1>, 2007.
- 598 Wu, G., Li, Z., Fu, C., Zhang, X., Zhang, R., Zhou, T., Li, J., Li, J., Zhou, D., Wu, L., Zhou, L.,  
599 He, B., Huang, R.: Advances in studying interactions between aerosols and monsoon in  
600 China. *Sci. China Earth Sci*, 59, 1–16, <https://doi.org/10.1007/s11430-015-5198-z>, 2016.
- 601 Xu, C., Ma, Y., You, C., and Zhu, Z.: The regional distribution characteristics of aerosol optical  
602 depth over the Tibetan Plateau, *Atmos. Chem. Phys.*, 15, 12065-12078,  
603 <https://doi.org/10.5194/acp-15-12065-2015>, 2015.
- 604 Yang, X., Zhao, C., Luo, N., Zhao, W., Shi, W., and Yan, X.: Evaluation and Comparison of  
605 Himawari-8 L2 V1. 0, V2. 1 and MODIS C6. 1 aerosol products over Asia and the Oceania  
606 regions, *Atmos. Environ.*, 220, 117068, <https://doi.org/10.1016/j.atmosenv.2019.117068>,  
607 2020.
- 608 Yang, Y., Ni, C., Jiang, M., and Chen, Q.: Effects of aerosols on the atmospheric boundary layer  
609 temperature inversion over the Sichuan Basin, China, *Atmos. Environ.*, 262, 118647,  
610 <https://doi.org/10.1016/j.atmosenv.2021.118647>, 2021.
- 611 Yao, T., Thompson, L.G., Mosbrugger, V., Zhang, F., Ma, Y., Luo, T., Xu, B., Yang, X., Joswiak,  
612 D.R., Wang, W., Joswiak, M.E., Devkota, L.P., Tayal, S., Jilani, R., Fayziev, R.: Third pole  
613 environment (TPE), *Environ. Dev.*, 3, 52-64, <https://doi.org/10.1016/j.envdev.2012.04.002>,  
614 2012.
- 615 Zhao, C., Yang, Y., Fan, H., Huang, J., Fu, Y., Zhang, X., Kang, S., Cong, Z., Letu, H., Menenti,  
616 M.: Aerosol characteristics and impacts on weather and climate over the Tibetan Plateau, *Natl.*  
617 *Sci. Rev.*, 7, 492-495, <https://doi.org/10.1093/nsr/nwz184>, 2020.



- 618 Zhao, P., Xu, X., Chen, F., Guo, X., Zheng, X., Liu, L., Hong, Y., Li, Y., La, Z., and Peng, H.:  
619 The third atmospheric scientific experiment for understanding the earth–atmosphere coupled  
620 system over the Tibetan Plateau and its effects, *B. Am. Meteorol. Soc.*, 99, 757–776,  
621 <https://doi.org/10.1175/BAMS-D-16-0050.1>, 2018.
- 622 Zhou, X., Bei, N., Liu, H., Cao, J., Xing, L., Lei, W., Molina, L. T., and Li, G.: Aerosol effects on  
623 the development of cumulus clouds over the Tibetan Plateau, *Atmos. Chem. Phys.*, 17, 7423–  
624 7434, <https://doi.org/10.5194/acp-17-7423-2017>, 2017.
- 625 Zhu, J., Xia, X., Che, H., Wang, J., Cong, Z., Zhao, T., Kang, S., Zhang, X., Yu, X., and Zhang,  
626 Y.: Spatiotemporal variation of aerosol and potential long-range transport impact over the  
627 Tibetan Plateau, China, *Atmos. Chem. Phys.*, 19, 14637–14656, [https://doi.org/10.5194/acp-](https://doi.org/10.5194/acp-19-14637-2019)  
628 19-14637-2019, 2019.



629 **Author contribution**

630 Mengjiao Jiang: Conceptualization, investigation, writing and editing, and funding acquisition.

631 Yaoting Li: Visualization, and editing.

632 Weiji Hu: Investigation, and simulation.

633 Yinshan Yang: Editing.

634 Guy Brasseur: Conceptualization, supervision, and editing.

635

636 **Declaration of interests**

637

638  The authors declare that they have no known competing financial interests or personal  
639 relationships that could have appeared to influence the work reported in this paper.

640

641  The authors declare the following financial interests/personal relationships which may be  
642 considered as potential competing interests:

643